2019

Deep-turbulence Wavefront Sensing using Digital Holography in the On-axis Phase Shifting Recording Geometry with Comparisons to the Self-referencing Interferometer

Douglas E. Thornton

Mark F. Spencer
Air Force Research Laboratory

Glen P. Perram
Air Force Institute of Technology

Research Article Vol. 58, No. 5 / 10 February 2019 / Applied Optics A179

applied optics

Deep-turbulence wavefront sensing using digital holography in the on-axis phase shifting recording geometry with comparisons to the self-referencing interferometer

Douglas E. Thornton,[1,*] Mark F. Spencer,[1,2] and Glen P. Perram[1]

[1]Air Force Institute of Technology, Department of Engineering Physics, 2950 Hobson Way Wright-Patterson Air Force Base, Dayton, Ohio 45433, USA
[2]Air Force Research Laboratory, Directed Energy Directorate, 3550 Aberdeen Ave SE, Kirtland Air Force Base, Albuquerque, New Mexico 87117, USA
*Corresponding author: douglas.thornton@afit.edu

Received 28 September 2018; revised 4 December 2018; accepted 5 December 2018; posted 5 December 2018 (Doc. ID 346495); published 15 January 2019

In this paper, we study the use of digital holography in the on-axis phase-shifting recording geometry for the purposes of deep-turbulence wavefront sensing. In particular, we develop closed-form expressions for the field-estimated Strehl ratio and signal-to-noise ratio for three separate phase-shifting strategies—the four-, three-, and two-step methods. These closed-form expressions compare favorably with our detailed wave-optics simulations, which propagate a point-source beacon through deep-turbulence conditions, model digital holography with noise, and calculate the Monte Carlo averages associated with increasing turbulence strengths and decreasing focal-plane array sampling. Overall, the results show the four-step method is the most efficient phase-shifting strategy and deep-turbulence conditions only degrade performance with respect to insufficient focal-plane array sampling and low signal-to-noise ratios. The results also show the strong reference beam from the local oscillator provided by digital holography greatly improves performance by tens of decibels when compared with the self-referencing interferometer.

https://doi.org/10.1364/AO.58.00A179

1. INTRODUCTION

Holography has a rich history in applications involving long-range imaging [1] and wavefront reconstruction [2]. In practice, we can use these applications in concert to overcome atmospheric distortions [3–5]. With the advent of robust focal-plane arrays (FPAs), researchers began to measure and store holograms digitally [6]. In an effort to characterize the atmosphere [7–9], this early research provided the framework needed for deep-turbulence wavefront sensing using digital holography.

Many applications, such as free-space laser communications, involve propagation paths which experience deep-turbulence conditions. Also known as distributed-volume turbulence or strong turbulence, deep turbulence arises from atmospheric aberrations being distributed along the propagation path. Given spatially coherent light, this outcome gives rise to time-varying constructive and destructive interference. Known as scintillation, this phenomenon typically hinders wavefront-sensing performance. While all atmospheric-optical paths experience scintillation to some degree, the effects of scintillation are often negligible for the vertical-propagation paths (e.g., those associated with ground-based telescopes [10], which experience weak-turbulence conditions) and often appreciable for the horizontal-propagation paths (e.g., those associated with long-range imaging systems [11], which experience deep-turbulence conditions).

Traditional wavefront-sensing methods use localized irradiance measurements to estimate phase gradients [e.g., the Shack–Hartmann wavefront sensor (SHWFS)]. Note that these traditional methods enable near-diffraction-limited optical systems [10]; however, performance degrades substantially in the presence of strong scintillation. For all intents and purposes, strong scintillation occurs when, for example, the log-amplitude variance, which gives a measure for the amount of scintillation, becomes greater than 0.2 [12,13]. Given strong scintillation, branch points arise in the continuous-phase function, in particular, where there are amplitude nulls in the real and imaginary parts of the complex-optical field [14]. For gradient-based wavefront sensors, like the SHWFS, these amplitude nulls cause the wavefront sensor to measure and reconstruct noise. The branch points also add a rotational

component to the phase function that gets mapped to the null space of a least-squares phase reconstructor, which manipulates the estimated phase gradients into a continuous-phase function. In turn, traditional wavefront-sensing methods do not perform well in deep-turbulence conditions.

We can alternatively use interferometric wavefront-sensing methods, such as the point-diffraction interferometer [15] and self-referencing interferometer (SRI) [16], to obtain an estimate of the complex-optical field. This estimate gives us access to the wrapped-phase function which contains both the irrotational and rotational phase components [14]. As such, we can use a branch-point-tolerant phase reconstructor to buy back performance when in the presence of strong scintillation [17]; however, this approach has yet to be demonstrated beyond a scaled-laboratory environment [18]. This last detail is most likely due to additional constraints caused by deep-turbulence conditions. For example, with an SRI, the received light is split to create a spatially filtered reference beam. Typically, researchers perform this spatial filtering by coupling the split received light into a single-mode optical fiber. When in the presence of strong scintillation, which arises with deep-turbulence conditions, this coupling results in efficiency losses and creates low signal-to-noise ratios (SNRs) that quickly lead to performance degradations [19].

To overcome the performance degradations caused by deep-turbulence conditions, we can instead use digital holography which is another interferometric wavefront-sensing method. In practice, digital holography is able to resolve the branch points associated with strong scintillation, since it provides us with an estimate of complex-optical field and access to the wrapped-phase function, which contains both the rotational and irrotational phase components [14]. Furthermore, digital holography is robust against the amplitude nulls caused by strong scintillation. The use of a strong reference beam from a local oscillator (LO) allows us to approach the shot-noise limit, since the signal beam is boosted above the read-noise floor of the FPA [20]. With these benefits in mind, this paper evaluates the performance of digital holography in the on-axis phase-shifting recording geometry (PSRG), as shown in Figs. 1 and 2. This paper, in turn, provides the necessary analysis needed to design and conduct future deep-turbulence experiments using digital holography in the on-axis PSRG. These experiments shall investigate both open- and closed-loop performance in scaled-laboratory and field environments. Such experiments shall also include additional factors not

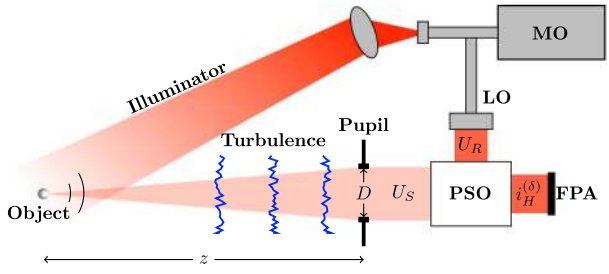

Fig. 1. Illustration of digital holography in the on-axis PSRG. Note that we need phase-shifting optics (PSO) to implement our phase-shifting strategy (cf. Fig. 2).

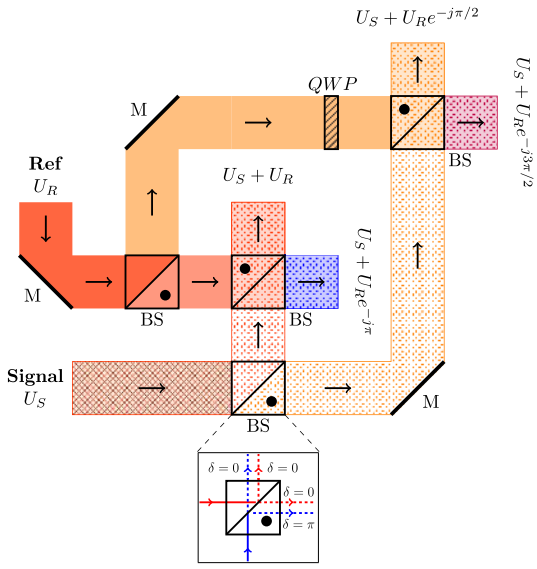

Fig. 2. Example of the PSO needed for the four-step method. This example also contains an illustration of the directional dependence of the π-phase shift upon reflection from a beam splitter (BS).

investigated in this paper, such as reference-beam nonuniformity, detector nonlinearities, laser practicalities, and vibration resistance.

It is worth mentioning that this paper builds upon the noiseless analysis contained in a recent conference proceeding by Thornton *et al.* [21]. Specifically, this paper develops and verifies the use of closed-form expressions for the SNR and field-estimated Strehl ratio with respect to the on-axis PSRG operating with three separate phase-shifting strategies—the four-, three-, and two-step methods [22,23]. Using detailed wave-optics simulations, which propagate a point-source beacon through deep-turbulence conditions, model digital holography with noise, and calculate the Monte Carlo averages associated with increasing turbulence strengths and decreasing focal-plane array sampling, the analysis shows the four-step method is the most efficient phase-shifting strategy. Furthermore, deep-turbulence conditions only degrade performance with respect to insufficient FPA sampling and low SNRs.

It is also worth mentioning that this paper is a "companion paper" to the analysis presented by Spencer *et al.* [24] and Banet *et al.* [25] with respect to digital holography in the off-axis image plane recording geometry (IPRG) and off-axis pupil plane recording geometry (PPRG), respectively. In practice, the off-axis IPRG and off-axis PPRG indirectly obtain an estimate of the complex-optical field from Fourier transformations and digital-signal-processing techniques (i.e., filtering the 2D spectrum of the digital hologram recorded with the FPA). Conversely, the on-axis PSRG directly obtains an estimate of the complex-optical field from multiple digital holograms being recorded on one or more FPA(s) and straightforward calculations [20].

In what follows, this paper develops closed-form expressions for two performance metrics (cf. Section 2), the SNR and field-estimated Strehl ratio, and verifies their use with detailed wave-optics simulations, which again, propagate a point-source

beacon through deep-turbulence conditions, model digital holography with noise, and calculate the Monte Carlo averages associated with increasing turbulence strengths and decreasing focal-plane array sampling. (cf. Section 3). This outcome demonstrates the on-axis PSRG is another valid recording geometry for deep-turbulence wavefront sensing. Before moving onto the next section, it is important to note that digital holography in the on-axis PSRG and the SRI are similar in design, except for the origin of the reference beam. Therefore, this paper also includes a comparison between digital holography in the on-axis PSRG and the SRI to show the benefits of using a strong reference beam for applications involving deep-turbulence conditions (cf. Section 4).

2. DEVELOPMENT OF CLOSED-FORM EXPRESSIONS FOR TWO PERFORMANCE METRICS

This section provides an overview of the optical setup used for digital holography in the on-axis PSRG. It also develops estimate and noise models for three separate phase-shifting strategies—the four-, three-, and two-step methods. We then use the models to develop closed-form expressions for the SNR and field-estimated Strehl ratio. In the ensuing sections, we verify the use of these performance metrics via wave-optics simulations and then use them to compare the performance of digital holography in the on-axis PSRG to the performance of an SRI, both using the four-step method (i.e., the most efficient method).

A. Optical Setup

As shown in Fig. 1, to realize digital holography in the on-axis PSRG, we split a master oscillator laser into two optical legs. The first leg flood illuminates an unresolved, ball-bearing object creating a point-source beacon. Then, the reflected spherical wave propagates through deep-turbulence conditions and becomes the signal beam U_S collimated in a pupil. The second leg creates a LO that gives rise to a reference beam U_R. After the reference and signal beams pass through the phase-shifting optics (PSO), we use the interference of light to create multiple holograms and record the resulting hologram irradiances $i_H^{(\delta)}$ on the FPA(s).

With Fig. 1 in mind, we show some of the details of the PSO in Fig. 2 for the four-step method. As shown in Fig. 2, the purpose of the PSO is to obtain the desired phase shift δ on the reference beam for the recorded holograms. Note that, in practice, a phase shift of π occurs with reflections from the mirrors (M) and 50/50 beam splitters when the light is incident on the side favoring the black dot. The reflected light incident on the opposing side of the black dot does not incur a phase shift [26]. Additionally, we obtain a $\pi/2$-phase shift at the quarter-wave plate. Aggregating these phase shifts for the reference and signal beams results in the four holograms shown in Fig. 2 and has been demonstrated in hardware [27,28].

There are two more items to consider with respect to Fig. 2: optical-path length and polarization. As shown, we do not draw the optical-path lengths to scale, and in a real system, we would want to match the optical-path lengths to ensure the proper phase shifts and minimize any losses in fringe visibility due to vibrations. Also note that we would need to image the signal and reference beams onto the FPA(s) to record the resulting hologram irradiances. To do so, we would need to employ relay optics (not shown here) to create conjugate pupil planes at the FPA(s), so that we conserve the phase of the signal and reference beams in forming our holograms. With respect to the polarization concerns, maximum fringe visibility only occurs when the reference and signal beam's polarization states match. However, in a real system, the reference beam's polarization state is probably different than the signal beam's polarization state due to rough-surface scattering from the object. Therefore, also not shown here are the polarization optics we would need to use to maximize the fringe visibility in our holograms. Moving forward in the analysis, we simply assume that we match the polarization states and that we are only dealing with absolute phase shifts (e.g., there are no piston errors in the phase shifts).

With the above assumptions in mind, the on-axis PSRG can employ different phase-shifting strategies to calculate the complex-optical field [22,23]. In this paper, we analyze three methods, namely, the four-, three-, and two-step methods. As previously stated, we show the four-step method's PSO in Fig. 2. The three- and two-step methods use similar PSO with some exceptions. In particular, we can modify the fraction of transmitted/reflected light off the first beam splitter encountered for the reference and signal beams to ensure equal amounts of light for each hologram. We can also exchange the final beam splitters with beam-combining optics to remove the unnecessary measurements while preserving the signal beam. In so doing, we only divide the signal beam by the number of holograms desired, and the holograms make use of corresponding strong reference beams to maximize SNR.

B. Estimate Model

Provided Figs. 1 and 2, the hologram irradiances $i_H^{(\delta)}$ take the following form:

$$\begin{aligned} i_H^{(\delta)} &= |U_S + U_R e^{-j\delta}|^2 \\ &= |U_S|^2 + |U_R|^2 + U_S U_R^* e^{j\delta} + U_S^* U_R e^{-j\delta}, \end{aligned} \tag{1}$$

where δ is again the desired reference-beam phase shift. Throughout the analysis, it is important to note that we assume, by choice, a spatially uniform reference beam. With increments of $\pi/2$ phase shifts, the corresponding $i_H^{(\delta)}$ become

$$\begin{aligned} i_H^{(0)} &= |U_S|^2 + |U_R|^2 + U_S U_R^* + U_S^* U_R, \\ i_H^{(\pi/2)} &= |U_S|^2 + |U_R|^2 + jU_S U_R^* - jU_S^* U_R, \\ i_H^{(\pi)} &= |U_S|^2 + |U_R|^2 - U_S U_R^* - U_S^* U_R, \\ i_H^{(3\pi/2)} &= |U_S|^2 + |U_R|^2 - jU_S U_R^* + jU_S^* U_R. \end{aligned} \tag{2}$$

Here, we replace the superscript δ with the appropriate reference-phase shift and $*$ denotes complex conjugate.

Provided Eq. (2), we can perform algebraic manipulations to isolate the signal beam U_S [22]. For each of the phase-shifting strategies considered in this paper, we arrive at the following relationships:

$$4U_R^* U_S = (i_H^{(0)} - i_H^{(\pi)}) - j(i_H^{(\pi/2)} - i_H^{(3\pi/2)}) \tag{3}$$

for the four-step method,

$$4U_R^* U_S = (1+j)(i_H^{(0)} - i_H^{(\pi/2)}) + (j-1)(i_H^{(\pi)} - i_H^{(\pi/2)}) \quad (4)$$

for the three-step method, and

$$2U_R^* U_S = (i_H^{(0)} - |U_S|^2 - |U_R|^2) - j(i_H^{(\pi/2)} - |U_S|^2 - |U_R|^2) \quad (5)$$

for the two-step method. Notice that the two-step method also requires that we know the irradiances associated with the signal and reference beams [cf. Eq. (5)]. To obtain the reference-beam irradiance, we would need to add a way to monitor the reference beam. This addition might seem excessive at first; however, in a real system, this monitoring would also allow us to maintain the strong reference beam assumption and avoid pixel saturation on the FPA(s). To obtain the signal-beam irradiance, we can make use of the following relationship derived by Poon and Liu [29]:

$$\begin{aligned} 2|U_S|^2 = {} & i_H^{(0)} + i_H^{(\pi/2)} \\ & - \{[2|U_R|^2 + i_H^{(0)} + i_H^{(\pi/2)}]^2 \\ & - 2[4|U_R|^4 + (i_H^{(0)})^2 + (i_H^{(\pi/2)})^2]\}^{1/2}. \end{aligned} \quad (6)$$

This relationship helps our efforts since the low signal levels associated with deep-turbulence conditions make the signal-beam irradiance hard to monitor.

With Eqs. (1)–(6) in mind, we can record the hologram irradiances $i_H^{(\delta)}$ with a FPA, which performs a pixel-by-pixel integration [20]. Thus, for a FPA with $M \times N$ pixels,

$$\begin{aligned} & \widehat{i}_H^{(\delta)}(nx_p, my_p) \\ & = \frac{1}{w_x w_y} \iint_{-\infty}^{\infty} i_H^{(\delta)}(x', y') \operatorname{rect}\left(\frac{x' - nx_p}{w_x}\right) \operatorname{rect}\left(\frac{y' - my_p}{w_y}\right) \mathrm{d}x' \mathrm{d}y', \end{aligned} \quad (7)$$

where m and n are the FPA pixel indices from $m = 1$ to M and $n = 1$ to N, x_p and y_p are the pixel pitches, w_x and w_y are the pixel widths, and

$$\operatorname{rect}(x) = \begin{cases} 1 & 0 \le |x| < 0.5 \\ 0.5 & |x| = 0.5 \\ 0 & |x| > 0.5 \end{cases} \quad (8)$$

is the rectangle function. Since the FPA detects photoelectrons [26,30], we determine the per-pixel mean number of hologram photoelectrons $\overline{m}_H(nx_p, my_p)$ as

$$\begin{aligned} \overline{m}_H^{(\delta)}(nx_p, my_p) &= \frac{\eta \tau w_x w_y}{h\nu} \widehat{i}_H^{(\delta)}(nx_p, my_p) \\ &= \frac{\eta \tau}{h\nu} i_H^{(\delta)}(nx_p, my_p) \\ &\quad * * \operatorname{rect}\left(\frac{nx_p}{w_x}\right) \operatorname{rect}\left(\frac{my_p}{w_y}\right), \end{aligned} \quad (9)$$

where η is the quantum efficiency, τ is the integration time, h is Planck's constant, ν is the optical frequency, and $**$ denotes 2D convolution. Similarly, we determine the per-pixel mean number of reference photoelectrons $\overline{m}_R$ as

$$\overline{m}_R = \frac{\eta \tau w_x w_y}{h\nu} |U_R|^2, \quad (10)$$

where again, we drop the pixel coordinates to denote spatial uniformity. The per-pixel mean number of signal photoelectrons $\overline{m}_S(nx_p, my_p)$ then becomes

$$\begin{aligned} \overline{m}_S(nx_p, my_p) &= \frac{\eta \tau}{h\nu} |U_S(nx_p, my_p)|^2 \\ &\quad * * \operatorname{rect}\left(\frac{nx_p}{w_x}\right) \operatorname{rect}\left(\frac{my_p}{w_y}\right). \end{aligned} \quad (11)$$

We will use these last two relationships in the coming noise model analysis.

Provided the right-hand sides of Eqs. (3)–(5), which depend on the measured hologram irradiances, $i_H^{(\delta)}$, we can use Eq. (9) to obtain a generic expression for the signal-beam estimate, $\widehat{U}_S^{(s)}$, in terms of the left-hand sides of Eqs. (3)–(5). In particular,

$$\begin{aligned} \widehat{U}_S^{(s)}(nx_p, my_p) &= \frac{\kappa}{\sqrt{s}} \frac{\eta \tau}{h\nu} U_R^* U_S(nx_p, my_p) \\ &\quad * * \operatorname{rect}\left(\frac{nx_p}{w_x}\right) \operatorname{rect}\left(\frac{my_p}{w_y}\right), \end{aligned} \quad (12)$$

where s is the number of shifts or measurements required by the phase-shifting strategy (e.g., $s = 4$, 3, and 2 for the four-, three-, and two-step methods, respectively) and κ is a phase-shifting constant, such that $\kappa = 4$ for the four- and three-step methods and $\kappa = 2$ for the two-step method [cf. the left-hand sides of Eqs. (3)–(5)]. In using Eq. (12) along with Eqs. (3)–(5), we define the magnitude of the signal beam at the pupil before the PSO [hence the exclusion of s and κ in Eq. (11)], so that we can easily compare the three methods. Also note that we define the magnitude of the reference beam at the FPA(s), since we can easily adjust the strength of the reference beam using

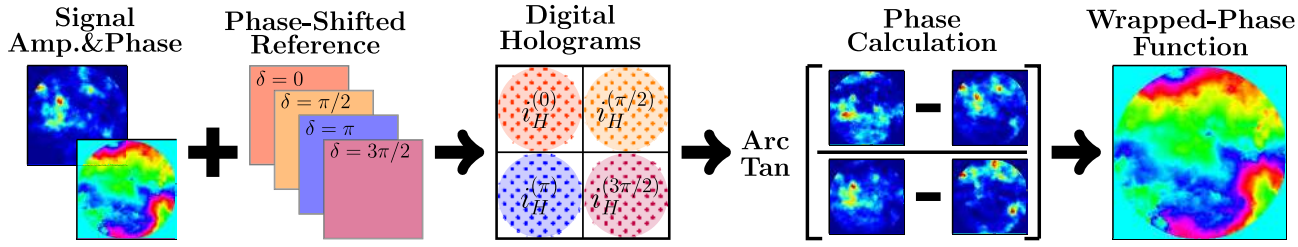

Fig. 3. Illustration of how digital holography in the on-axis PSRG allows us to access the wrapped-phase function. Here, we use the interference of light to create multiple holograms by mixing a phase-shifted reference beam with a signal beam. Note that the number of shifts or measurements required by the phase-shifting strategy is dependent on the phase-shifting method being used (here, we illustrate the four-step method). After we record the hologram irradiances with a FPA, we perform a straightforward calculation to obtain the wrapped-phase function from an estimate of complex-optical field [cf. Eq. (12) along with Eqs. (3)–(5)].

the LO (cf. Figs. 1 and 2). As such, we are left with a straightforward calculation to obtain the wrapped-phase function from an estimate of the complex-optical field. We illustrate this process for the four-step method in Fig. 3.

C. Noise Model

Moving forward in the analysis, we would like to account for the effects of shot noise and read noise. For this purpose, we assume that the shot noise results from the random arrival times of the photons that are incident on the FPA, and that the read noise results from the read-out integrated circuitry of the FPA. We also assume that the shot noise follows a Poisson distribution, whereas read noise follows a Gaussian distribution.

For a Poisson-distributed random process, the mean is equal to the variance [26]. In this paper [cf. Eqs. (10) and (11)], the mean is equal to the sum of the per-pixel mean number of photoelectrons from the signal and reference beams, $\overline{m}_S$ and $\overline{m}_R$, respectively. Here, we drop the FPA coordinates to denote the average over the entire detection area. Since we set $\overline{m}_R$ to 75% of pixel-well depth of the FPA, we assume that $\overline{m}_R \gg \overline{m}_S$ and that the mean number of hologram photoelectrons varies little from pixel to pixel because of the strong reference beam ($\overline{m}_H \approx \overline{m}_R$). In turn, the Poisson-distributed shot noise follows a Gaussian distribution (to a good approximation when $\overline{m}_R \gg 1$) with variance $\overline{m}_R + \overline{m}_S \approx \overline{m}_R$. Armed with these assumptions, we can add the variances for each Gaussian-distributed random process and arrive at the noise variance σ_n^2, such that

$$\sigma_n^2 = \overline{m}_R + \sigma_r^2, \tag{13}$$

where σ_r^2 is the variance of the read noise.

In the analysis that follows, we model the additive Gaussian noise [20], such that

$$\overline{m}_{H+N}^{(\delta)}(nx_p, my_p) = \overline{m}_H^{(\delta)}(nx_p, my_p) + \sigma_n n_k(nx_p, my_p), \tag{14}$$

where $\overline{m}_{H+N}^{(\delta)}$ is the mean number of hologram photoelectrons with noise and $n_k(nx_p, my_p)$ is the k^{th} realization of real-valued, zero-mean, unit-variance Gaussian random numbers. Correspondingly, the signal-beam estimate with noise $U_{S+N}^{(s)}$ takes the following form:

$$\widehat{U}_{S+N}^{(s)}(nx_p, my_p) = \widehat{U}_S^{(s)}(nx_p, my_p) + \sqrt{\zeta}\sigma_n N_k(nx_p, my_p), \tag{15}$$

where ζ is a constant resulting from the number of noise-contributing terms in Eqs. (3)–(5) (i.e., $\zeta = 4$ for the four- and two-step methods and $\zeta = 8$ for the three-step method), σ_n^2 is the noise variance [cf. Eq. (13)], and $N_k(nx_p, my_p)$ is the k^{th} realization of circular-complex Gaussian random numbers with zero mean and unit variance. In the signal-beam estimate, $\widehat{U}_S^{(s)}$ [cf. Eq. (12)], each measured hologram irradiance, $i_H^{(\delta)}$, adds to the total noise of the estimate and ζ accounts for this addition. Lastly, we state that $\zeta = 4$ for the two-step method; however, Eq. (5) has six terms. Since we assume $\overline{m}_R \gg \overline{m}_S$, the noise from the signal-beam irradiance ($|U_S|^2$) is negligible and even more so with the use of Eq. (6). This assumption is a sound one, as shown in the following analysis.

D. Signal-to-Noise and Field-Estimated Strehl Ratios

In what follows, we formulate the SNR $S/N^{(s)}$ as the ratio of the mean signal power to the total noise variance. As such, we obtain the following relationship:

$$S/N^{(s)} = \frac{\langle |\widehat{U}_S^{(s)}(x,y)|^2 \rangle}{\mathcal{V}\{\widehat{U}_{S+N}^{(s)}(x,y)\}}, \tag{16}$$

where $\langle \cdot \rangle$ denotes mean over all pixels, $\widehat{U}_S^{(s)}$ is the signal-beam estimate [cf. Eq. (12)], $\mathcal{V}\{\cdot\}$ denotes the variance operator over all pixels, and $\widehat{U}_{S+N}^{(s)}$ is the is the signal-beam estimate with noise [cf. Eq. (15)]. Here, we again drop the FPA coordinates to denote the average over the entire detection area. Provided Eq. (16) along with Eqs. (10)–(12), we then determine the mean-signal power as

$$\langle |\widehat{U}_S^{(s)}(x,y)|^2 \rangle = \frac{\kappa^2}{s}\overline{m}_R\overline{m}_S, \tag{17}$$

and the total noise variance as

$$\mathcal{V}\{\widehat{U}_{S+N}^{(s)}(x,y)\} = \zeta\sigma_n^2. \tag{18}$$

Substituting Eqs. (17) and (18) into Eq. (16), we obtain the following closed-form expressions for the SNR:

$$S/N^{(4)} = \frac{\overline{m}_R\overline{m}_S}{\overline{m}_R + \sigma_r^2} \tag{19}$$

for the four-step method,

$$S/N^{(3)} = \frac{2}{3}\frac{\overline{m}_R\overline{m}_S}{\overline{m}_R + \sigma_r^2} \tag{20}$$

for the three-step method, and

$$S/N^{(2)} = \frac{1}{2}\frac{\overline{m}_R\overline{m}_S}{\overline{m}_R + \sigma_r^2} \tag{21}$$

for the two-step method. If $\overline{m}_R \gg \sigma_r^2$, then we reach the shot-noise limit and these closed-form expressions become a function of only $\overline{m}_S$. In turn, these closed-form expressions for the SNR provide a nice metric for the performance of digital holography in the on-axis PSRG.

Another performance metric of interest in the analysis is the field-estimated Strehl ratio $S_F^{(s)}$ [24,25,31]. As shown in Appendix A and Appendix B, we can relate $S_F^{(s)}$ to the SNR $S/N^{(s)}$ via the following relationship [31]:

$$S_F^{(s)} = \frac{1}{1 + \frac{1}{S/N^{(s)}}}. \tag{22}$$

Provided Eq. (22) along with Eqs. (19)–(21), we obtain the following closed-form expressions for field-estimated Strehl ratio:

$$S_F^{(4)} = \frac{\overline{m}_R\overline{m}_S}{\overline{m}_R\overline{m}_S + \overline{m}_R + \sigma_r^2} \tag{23}$$

for the four-step method,

$$S_F^{(3)} = \frac{2\overline{m}_R\overline{m}_S}{2\overline{m}_R\overline{m}_S + 3(\overline{m}_R + \sigma_r^2)}, \tag{24}$$

for the three-step method, and

$$S_F^{(2)} = \frac{\overline{m}_R\overline{m}_S}{\overline{m}_R\overline{m}_S + 2(\overline{m}_R + \sigma_r^2)}, \tag{25}$$

for the two-step method. We verify the use of these closed-form expressions in the next section.

3. PERFORMANCE METRIC COMPARISON USING WAVE-OPTICS SIMULATIONS

This section develops the wave-optics simulations employed to verify the closed-form expressions developed above for the signal-to-noise and field-estimated Strehl ratios. We conduct this analysis entirely in MATLAB using the principles from Schmidt [32] with help from WaveProp [33] and AOTools [34], which are MATLAB toolboxes written by the Optical Sciences Company. For further insight on these wave-optics simulations, we list several references that include additional detail [21,24,25,35,36].

A. Numerical Model

With Fig. 1 in mind, we modeled the point-source beacon as a narrow sinc function modulated by a raised-cosine envelope on a 4096×4096 numerical grid. Note that we set the physical side length of the numerical grid in the object plane, so that we met Fresnel scaling. We then propagated the point-source beacon to the pupil plane using the split-step beam propagation method. Here, we collimated the light and cropped the numerical grid to 256×256, so that it had the same physical side length as the pupil diameter, D. We provide a list of simulation parameters in Table 1.

With Table 1 in mind, we modeled five distinct scenarios with increasing turbulence strengths. Table 2 lists the refractive-index structure parameter, C_n^2, spherical-wave log amplitude variance (Rytov number), $\sigma_{\chi\text{-}sw}^2$, and spherical-wave coherence length (Fried parameter), $r_{0\text{-}sw}$, for the various scenarios. For a given C_n^2, wavelength λ, and horizontal-path propagation distance z, we can calculate $\sigma_{\chi\text{-}sw}^2$ and $r_{0\text{-}sw}$, respectively, using the following formulas [37]:

$$\sigma_{\chi\text{-}sw}^2 = 0.124 k^{7/6} z^{11/6} C_n^2 \tag{26}$$

and

$$r_{0\text{-}sw} = 0.33 \left(\frac{\lambda^2}{z C_n^2} \right)^{3/5}, \tag{27}$$

where $k = 2\pi/\lambda$ is the angular wavenumber. Provided Eqs. (26) and (27), the turbulence strength becomes proportional to the Rytov number and inversely proportional to the Fried parameter. Recall for imaging systems, the Fried parameter provides a measure for resolution relative to the pupil diameter D; therefore, the larger, the better. Additionally, the Rytov number provides a measure for the amount of scintillation. As a rule of thumb, Rytov numbers less than 0.2 provide weak scintillation and those greater than 0.2 provide strong scintillation. As shown in Table 2, the turbulence strength increases from Scenario 1 to Scenario 5.

With respect to the split-step beam propagation method, we used 10 equally spaced Kolmogorov phase screens to achieve deep-turbulence conditions. By satisfying Fresnel scaling, we met all of the sampling requirements set forth by Schmidt [32], as discussed in Thornton *et al.* [21]. For model verification, the discrete calculations were within 1% error when compared to the continuous calculations [cf. Eq. (26) and (27)]. Additionally, we calculated the Monte Carlo averages associated with the magnitude of the complex degree of coherence in the pupil plane using 40 independent realizations for Scenarios 1–5 in Table 2, and the results closely matched theory [21]. We show an example of one realization of the irradiance and wrapped phase in Fig. 4 for the simulated signal-beam truth.

In addition to the turbulence strength, we varied the FPA sampling by changing the number of FPA pixels across a demagnified pupil image. For this objective, we interpolated the simulated signal beam in the pupil plane to match the size of the FPA. Note that we fixed the square-pixel width, so that the physical size of the FPA was proportional to the number of pixels across. Therefore, we demagnified the simulated signal beam, such that $M_T = W/D$, where M_T is the transverse magnification, $W = N_p w_{x,y}$ is the side length of the FPA, N_p is the FPA sampling, and $w_{x,y}$ is the square-pixel width. After this demagnification via interpolation, we scaled the mean number of signal photoelectrons $\overline{m}_S$ to vary the signal strength. For this purpose, we set the characteristics of the FPA, such that the quantum efficiency was 100%, as well as the pixel fill factor. Additionally, we assumed a uniform, linear pixel gain from zero to saturation (100,000 pe). As mentioned before, we then set the read-noise standard deviation, such that $\sigma_r = 100$ pe, and the strength of the simulated strong reference beam, so that $\overline{m}_R = 75{,}000$ pe. Put another way, we set the mean number of reference photoelectrons $\overline{m}_R$ to 75% of pixel-well depth of the FPA to create a strong reference beam but avoid pixel saturation and excess shot noise.

Table 1. Simulation Parameters Used in the Wave-Optics Simulations

$\lambda = 1$ μm	optical wavelength
$D = 30$ cm	pupil diameter
$z = 7.5$ km	propagation distance
$h = 10$ m	horizontal-path altitude

Table 2. Turbulence Parameters Used for Five-Distinct Scenarios

Scenario	1	2	3	4	5
$C_n^2[m^{-2/3} \times 10^{-15}]$	1.00	1.50	2.00	2.50	3.00
$\sigma_{\chi\text{-}sw}^2$	0.135	0.202	0.270	0.337	0.404
$r_{0\text{-}sw}$[cm]	9.92	7.78	6.55	5.73	5.14

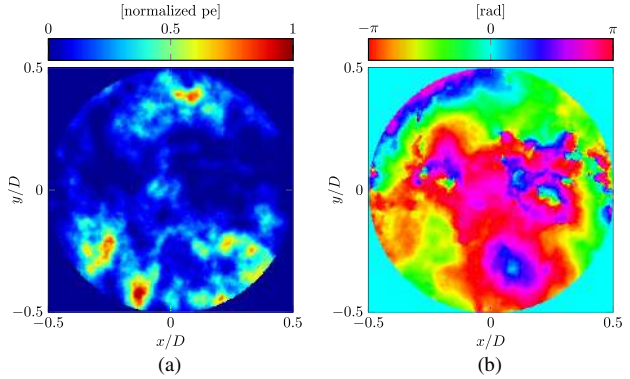

Fig. 4. (a) Irradiance and (b) wrapped phase for the simulated signal-beam truth for one realization of the turbulence (cf. Scenario 5 in Table 2).

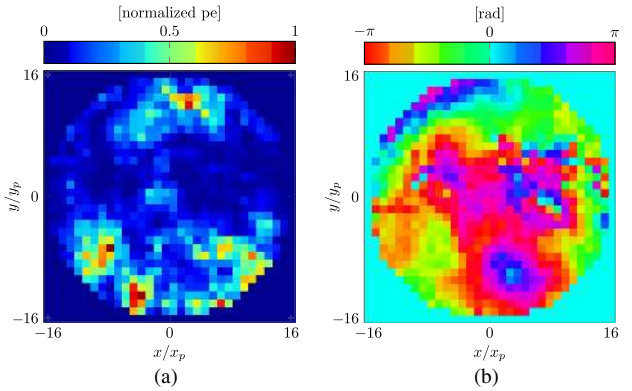

Fig. 5. (a) Irradiance and (b) wrapped phase for the simulated signal-beam estimate for one realization of turbulence (cf. Scenario 5 in Table 2).

We accounted for each phase-shifting strategy by dividing the simulated signal beam by the number of measurements needed for the corresponding method [cf. the factor s in Eq. (12)]. With this in mind, we then estimated the complex-optical field in the pupil plane with the corresponding pixel-by-pixel formulas [cf. Eq. (12) along with Eqs. (3)–(5)]. We show an example of one realization of the irradiance and wrapped phase in Fig. 5 for the simulated signal-beam estimate.

B. Numerical Results

The results of the wave-optics simulations presented here cover a threefold trade space with respect to the four-, three-, and two-step methods. In particular, we quantify performance by

1. varying the signal strength,
2. varying the turbulence strength, and
3. varying the FPA sampling.

As shown in Fig. 6, we verify the use of Eqs. (16)–(25). Here, we compare both the numerical field-estimated Strehl ratio S_F and numerical SNR S/N to theory. Note that the differences between the theoretical lines and data points are less than 1% for the Monte Carlo averages from 40 independent realizations of turbulence and 30 independent realizations of noise for all of the scenarios given in Table 2. To calculate S_F, we made use of the following relationship (cf. Appendix A):

$$S_F = \frac{|\langle U_S(x,y)\widehat{U}^*_{S+N}(x,y)\rangle|^2}{\langle|U_S(x,y)|^2\rangle\langle|\widehat{U}_{S+N}(x,y)|^2\rangle}, \tag{28}$$

where $U_S(x,y)$ is the signal-beam truth and $\widehat{U}_{S+N}(x,y)$ is the signal-beam estimate with noise. Similarly, to calculate S/N, we made use of the following relationship:

$$S/N = \frac{\langle|\widehat{U}_{S+N}|^2 - |\widehat{U}_N|^2\rangle}{\mathrm{Var}\{\widehat{U}_N\}}, \tag{29}$$

where $\widehat{U}_N$ is the noise estimate associated with reconstructing only the strong reference beam [cf. Eq. (12) along with Eqs. (3)–(5)].

With the results of Fig. 6 in mind, in Fig. 7 we compare the numerical field-estimated Strehl ratio S_F as a function of signal strength $\overline{m}_S$ to theory [cf. Eqs. (23)–(25)]. Again, the observed error between theory and the numerical results is less than 1% for the Monte Carlo averages from 40 independent realizations of turbulence and 30 independent realizations of noise for Scenario 1 and 5 in Table 2. From the results, we see that the four-step method is the most efficient phase-shifting strategy, despite having the most required signal-beam splits. The complete sampling of the phase in $\pi/2$ steps, in practice, results in a more precise estimate of the complex-optical field. Put another way, the ζ term within the total noise variance $\zeta\sigma_n$ [cf. Eq. (16)] introduces less noise into the estimate for the four-step method.

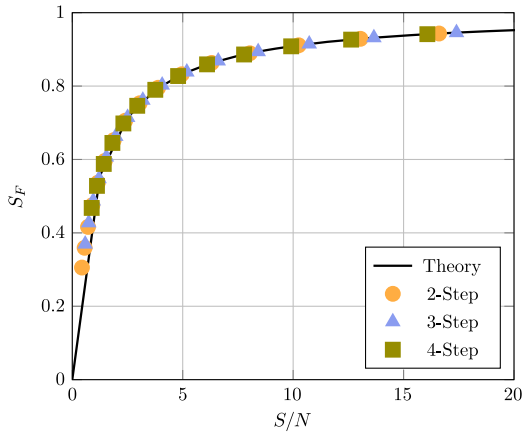

Fig. 6. Numerical field-estimated Strehl ratio S_F versus the numerical SNR S/N with a comparison to theory. Shown here are the Monte Carlo averages from 40 independent realizations of turbulence and 30 independent realizations of noise for all of the scenarios given in Table 2 and the three separate phase-shifting strategies of interest in this paper. Note that $N_p = 256$ for all of these results.

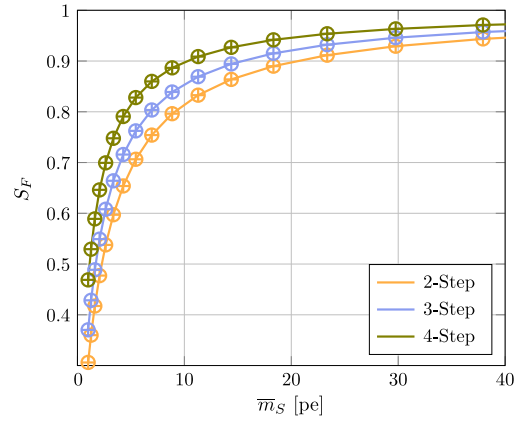

Fig. 7. Numerical field-estimated Strehl ratio S_F versus the signal strength $\overline{m}_S$ with a comparison to theory. Shown here are the Monte Carlo averages from 40 independent realizations of turbulence and 30 independent realizations of noise for Scenario 1 and Scenario 5 in Table 2 and the three separate phase-shifting strategies of interest in this paper. Note that $N_p = 256$ for all of these results. Also note that the open circles represent the results from Scenario 1, whereas the plus signs represent the results from Scenario 5.

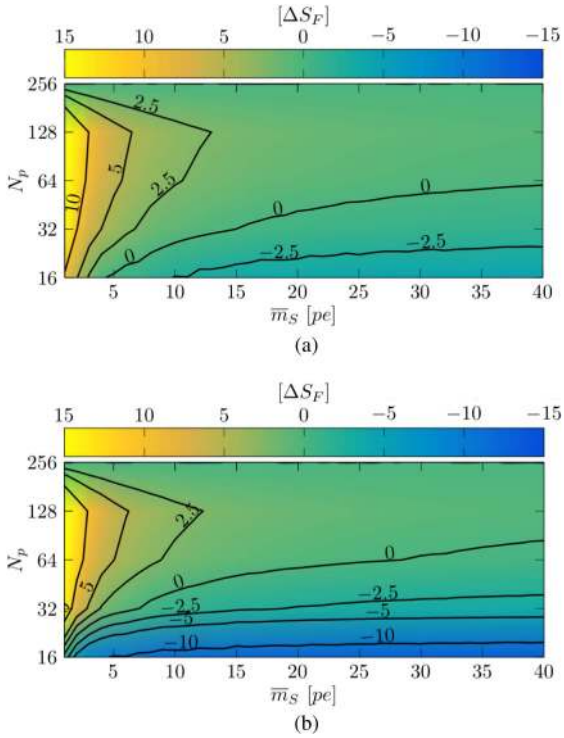

Fig. 8. Relative percent difference (ΔS_F) between the theoretical and numerical field-estimated Strehl ratios for (a) Scenario 1 and (b) Scenario 5 from Table 2. We plot the results as a function of the FPA sampling N_p and mean signal strength $\overline{m}_S$ for the four-step method [cf. Eq. (23)]. Shown here are the Monte Carlo averages from 40 independent realizations of turbulence and 30 independent realizations of noise.

It is important to note that the results contained in Figs. 6 and 7 made use of a FPA with 256 pixels across the simulated demagnified pupil image (i.e., $M_T = 1$). With that said, Fig. 8 shows the relative percent difference between the theoretical and numerical field-estimated Strehl ratios for Scenarios 1 and 5 from Table 2 and the four-step method. Here, M_T varied such that the modeled, square FPA size ranged from 16 to 256 pixels across (N_p), and as such, the signal-beam estimate's grid size varied from 16×16 to 256×256. To compare the signal-beam estimate to the simulated signal-beam truth (256 pixels across), we upsampled via linear interpolation. We plot the results as a function of the FPA sampling N_p (y axis) and the signal strength $\overline{m}_S$ (x axis). In Fig. 8, we calculate the relative percent difference as

$$\Delta S_F = \frac{S_F - S_F^{(4)}}{S_F^{(4)}} \times 100, \tag{30}$$

where $S_F^{(4)}$ is the theoretical result [cf. Eq. (23)]. Provided Eq. (30), positive values represent the case where $S_F > S_F^{(4)}$, whereas negative values represent the case where $S_F < S_F^{(4)}$.

With Fig. 8 in mind, a couple of features become apparent in the analysis. First, we reach steady-state differences between the theoretical and numerical results when $\overline{m}_S \gtrsim 10$, which is where the $S/N \gtrsim 10$ and $S_F \gtrsim 0.9$. As we increase the turbulence strength, the induced sampling errors also increase, and the results for Scenarios 2–4 also follow this trend. Thus, turbulence strength only affects the FPA sampling requirements. The largest differences occur with smaller values of N_p and stronger turbulence strengths. Second, at low SNRs ($S/N < 10$), the differences vary greatly with N_p. This outcome is due to the smoothing that occurs given the coarser FPA sampling [cf. the 2D convolution in Eq. (12)]. It also shows that when we properly sample the Fried parameter [cf. Eq. (27)], digital holography estimates the complex-optical field exceptionally well [38].

4. SRI COMPARISON

As discussed above, the SRI is an alternative interferometric wavefront-sensing method [16]. The primary difference between digital holography and the SRI is that the SRI splits the received signal beam to create a reference beam via spatial filtering, typically with a single-mode optical fiber. With that said, Rhoadarmer and Klein provide further discussion on the design of an SRI [28]. Various phase-shifting strategies also exist for the SRI, but similar to digital holography in the on-axis PSRG, the four-step method has the best performance [39].

In this section, we model deep-turbulence wavefront sensing using the SRI in the same fashion as the four-step method for digital holography in the on-axis PSRG (i.e., in an open-loop configuration) with a few exceptions. The first exception is that we set the beam-splitter ratio β, which splits the signal beam to create the reference beam, so that $\overline{m}_S = \overline{m}_R$. This choice maximizes the SNR [40]. Additionally, we include the effects of a fiber-coupling efficiency η_c. Wheeler and Schmidt [19] showed that this efficiency depends on the spatial coherence radius ρ_0 or the coherence length r_0, since $r_0 \approx 2.1\rho_0$ [41], relative to the pupil diameter D. From Table 2, the corresponding η_c for Scenario 1 and Scenario 5 is 10% and 1%, respectively. Therefore, in the analysis that follows, we make use of the following three cases: $\eta_c = 100\%$ for the ideal case, $\eta_c = 10\%$ for Scenario 1, and $\eta_c = 1\%$ for Scenario 5.

Because of the losses encountered with the fiber-coupling efficiency η_c, we need to introduce a new term: $\overline{m}_i$, which is the mean number of incident photoelectrons. For digital holography in the on-axis PSRG, $\overline{m}_i = \overline{m}_S$, since we use 100% of the signal beam. On the other hand, for the SRI, $\overline{m}_S = \beta\overline{m}_i$, which is the percent of the incident light split for the signal beam, and $\overline{m}_R = (1-\beta)\eta_c\overline{m}_i$, which is the percent of the incident light both split and coupled into the single-mode optical fiber for the reference beam. In turn, $\overline{m}_L = (1-\beta)(1-\eta_c)\overline{m}_i$ is the percent of the incident light lost due to fiber coupling, so that $\overline{m}_i = \overline{m}_S + \overline{m}_R + \overline{m}_L$ for the SRI.

Similar to the analysis presented above (cf. Section 2), Rhoadarmer and Barchers formulated closed-form expressions for the SRI [31]. With respect to the four-step method, the SNR $S/N_{SRI}^{(4)}$ and field-estimated Strehl ratio $S_{F,SRI}^{(4)}$ follow as

$$S/N_{SRI}^{(4)} = \frac{1}{4}\frac{\overline{m}_S^2}{\overline{m}_S/2 + \sigma_r^2}, \tag{31}$$

and

$$S_{F,SRI}^{(4)} = \frac{\overline{m}_S^2}{\overline{m}_S^2 + 2\overline{m}_S + 4\sigma_r^2}, \tag{32}$$

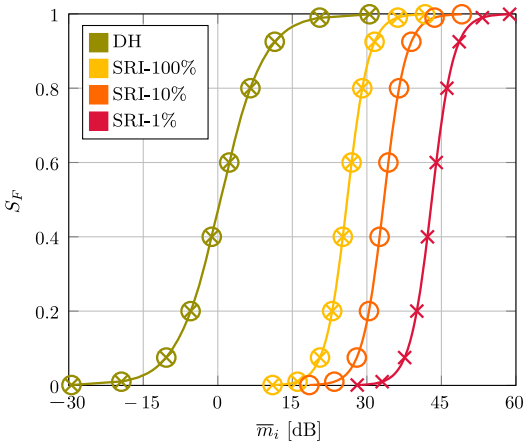

Fig. 9. Numerical field-estimated Strehl ratio S_F versus the mean number of incident photoelectrons $\overline{m}_i$ for digital holography in the on-axis PSRG and the SRI with 100%, 10%, and 1% fiber-coupling efficiency. Here, the solid lines represent the theoretical results for the four-step method [cf. Eq. (23) for digital holography in the on-axis PSRG and Eq. (32) for the SRI]. The open circles represent the numerical results for Scenario 1, whereas the x's represent the numerical results for Scenario 5 (cf. Table 2). Shown here are the Monte Carlo averages from 40 independent realizations of turbulence and 30 independent realizations of noise.

respectively. Provided Eqs. (31) and (32), we compare the performance of digital holography in the on-axis PSRG to the SRI.

For the comparison, we formulated results from two perspectives, as shown in Figs. 9 and 10. Here, we verified the use of the closed-form expressions for the SRI [cf. Eqs. (31) and (32)]. Note that the differences between the theoretical lines and data points are less than 1% for the Monte Carlo

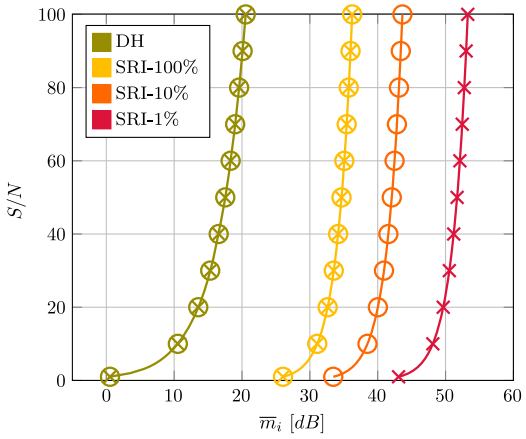

Fig. 10. Numerical SNR S/N versus the mean number of incident photoelectrons $\overline{m}_i$ for digital holography in the on-axis PSRG and the SRI with 100%, 10%, and 1% fiber-coupling efficiency. Here, the solid lines represent the theoretical results for the four-step method [cf. Eq. (19) for digital holography in the on-axis PSRG and Eq. (31) for the SRI). The open circles represent the numerical results for Scenario 1, whereas the x's represent the numerical results for Scenario 5 (cf. Table 2). Shown here are the Monte Carlo averages from 40 independent realizations of turbulence and 30 independent realizations of noise.

averages from 40 independent realizations of turbulence and 30 independent realizations of noise. Also, we made use of a FPA with 256 pixels across the simulated demagnified pupil image. With that said, the results show that digital holography in the on-axis PSRG outperforms the SRI with respect to the numerical field-estimated Strehl ratio S_F (cf. Fig. 9) and the numerical SNR S/N (cf. Fig. 10) by multiple orders of magnitude. As shown in Fig. 10, for example, there are notable differences in the incident mean number of incident photoelectrons $\overline{m}_i$ required to reach an $S/N = 10$ with approximately 21 dB difference for the ideal case (green to yellow), 28 dB difference for Scenario 1 (green to orange), and 37 dB difference for Scenario 5 (green to red). These differences represent the necessary SRI signal amplification needed to achieve similar performance to digital holography in the on-axis PSRG due to the lack of a strong reference beam from the LO provided by digital holography.

5. CONCLUSION

The results presented here showcase the strengths of digital holography in the on-axis PSRG for the purposes of deep-turbulence wavefront sensing. Throughout this paper, we develop closed-form expressions for the field-estimated Strehl and signal-to-noise ratios for the two-, three-, and four-step methods. Using detailed wave-optics simulations, which propagate a point-source beacon through deep-turbulence conditions, model digital holography with noise, and calculate the Monte Carlo averages associated with increasing turbulence strengths and decreasing focal-plane array sampling, we also verify the use of these closed-form expressions. Overall, the results show the four-step method is the most efficient phase-shifting strategy and deep-turbulence conditions only degrade performance with respect to insufficient FPA sampling and low SNRs.

The first result is somewhat counterintuitive since the four-step method requires the most signal-beam splits. However, the results of the closed-form expressions and detailed wave-optics simulations show the four-step method is more concise with less noise in estimating the complex-optical field. Furthermore, when the FPA sampling and SNR is sufficient, the percent difference between the theoretical results and the numerical results is negligible, regardless of the turbulence strength. In general, the results show when the FPA sampling is greater than 32 pixels and the SNR is greater than 10, the field-estimated Strehl ratios are greater than 0.9 (with respect to the four-step method).

A comparison to the SRI also shows the benefits of using a strong reference beam to perform interferometric wavefront sensing. For this purpose, we modeled the SRI in an ideal way and included the effects of a fiber-coupling efficiency to provide more realistic SNRs with increasing turbulence strengths. In the low-SNR regime, the SRI needs tens of decibels more signal-beam power to achieve similar performance to digital holography in the on-axis PSRG. As such, this comparison provides a performance benchmark for applications involving deep-turbulence conditions.

In summary, this paper evaluates the performance of digital holography in the on-axis PSRG and enables the optimal design

of such a deep-turbulence wavefront sensor. By employing four $\pi/2$ phase shifts, we minimized the total noise and improved system performance in terms of both the SNR and field-estimated Strehl ratio. System performance also approached theoretical limits when we sampled the four digital holograms with at least five pixels across the Fried parameter. Since digital holography provides a strong reference beam from a LO, we then showed it outperforms the SRI in low signal-to-noise conditions for deep-turbulence applications. In turn, this paper provides the necessary analysis needed to design and conduct future deep-turbulence experiments using digital holography in the on-axis PSRG.

APPENDIX A: FIELD-ESTIMATED STREHL RATIO

The field-estimated Strehl ratio S_F is a performance metric that allows us to investigate the estimation accuracy of the various interferometric wavefront sensing methods [15,24,25,31]. In practice, S_F results from the Cauchy–Schwartz Inequality, such that

$$|\langle U, V\rangle|^2 \le \langle U, U\rangle\langle V, V\rangle, \tag{A1}$$

where U and V are 2D arbitrary vectors in the field of complex numbers and $\langle\cdot,\cdot\rangle$ is the inner-product operator. By dividing both sides of Eq. (A1) by the right, we reach the following inequality:

$$1 \ge \frac{|\langle U, V\rangle|^2}{\langle U, U\rangle\langle V, V\rangle}, \tag{A2}$$

which gives the properties of a Strehl ratio. This inequality ranges from 1, when $U = V$, to 0, when U is orthogonal to V, and is proportional to the similarity between the two complex vectors. However, the definition of S_F uses expectation values instead of inner products. The inner product for the complex vectors here is

$$\langle U, V\rangle = \sum_{i,j=1}^{m,n} U_{ij} V_{ij}^*, \tag{A3}$$

where m, n is the number of elements in the corresponding i, j dimensions and the superscript $*$ denotes complex conjugate. We can ignore the customary transpose, since we desire a point-by-point comparison and linearize the 2D vectors to 1D space. In this particular case, the expectation value is mathematically similar to the inner product, such that

$$\langle UV^*\rangle = \frac{1}{mn}\sum_{i,j=1}^{m,n} U_{ij} V_{ij}^* = \frac{1}{mn}\langle U, V\rangle. \tag{A4}$$

Here, the nuance between the inner-product operator $\langle\cdot,\cdot\rangle$ and expectation-value operator $\langle\cdot\rangle$ is negligible in the calculation of S_F, since the factor of $1/(mn)^2$ cancels in the numerator from the denominator. If we substitute the two complex vectors U and V with $\widehat{U}_S$ for the truth complex-optical field and $\widehat{U}_{S+N}$ for the estimated complex-optical field with noise, then S_F becomes

$$S_F = \frac{|\langle \widehat{U}_S(x,y)\,\widehat{U}_{S+N}^*(x,y)\rangle|^2}{\langle|\widehat{U}_S(x,y)|^2\rangle\langle|\widehat{U}_{S+N}(x,y)|^2\rangle}. \tag{A5}$$

For all intents and purposes, we repeat Eq. (A5) above in Eq. (28).

APPENDIX B: FIELD-ESTIMATED STREHL RATIO AS A FUNCTION OF SNR

Rhoadarmer and Barchers [31] used the following relationship:

$$S_F = \frac{1}{1 + \frac{1}{S/N}} \tag{B1}$$

to write the field-estimated Strehl ratio S_F as a function of the SNR S/N. Here, we show how these two metrics are related in Eq. (B1). For this purpose, $\widehat{U}_S$ is the estimated complex-optical field and $\widehat{U}_{S+N}$ is the estimated complex-optical field with noise, such that

$$\widehat{U}_{S+N}(x,y) = \widehat{U}_S(x,y) + \frac{\sigma_n}{\sqrt{2}} N_k(x,y), \tag{B2}$$

where σ_n is the noise standard deviation and N_k is the kth realization of complex-circular Gaussian random numbers with zero mean and unit variance. Note that the factor of $\sqrt{2}$ in Eq. (B2) normalizes the variance since N_k has both real and imaginary parts. In turn, the numerator of S_F [cf. Eq. (A5)] follows as

$$|\langle \widehat{U}_S(x,y)\,\widehat{U}_{S+N}^*(x,y)\rangle|^2 = |\langle|\widehat{U}_S(x,y)|^2\rangle|^2, \tag{B3}$$

since the additive-noise term has zero mean. Recall that $|U_R| \gg |U_S(x,y)|$; thus, we can assume that $|\widehat{U}_S(x,y)| \approx |\widehat{U}_S|$ in writing Eq. (B3). The second term in the denominator of S_F then follows as

$$\langle|\widehat{U}_{S+N}(x,y)|^2\rangle = \langle|\widehat{U}_S(x,y)|^2\rangle + \sigma_n^2, \tag{B4}$$

where the cross terms go to zero, since again the additive-noise term has zero mean. Substituting Eqs. (B3) and (B4) into Eq. (A5), the new form of S_F becomes

$$S_F = \frac{|\langle|\widehat{U}_S(x,y)|^2\rangle|^2}{\langle|\widehat{U}_S(x,y)|^2\rangle(\langle|\widehat{U}_S(x,y)|^2\rangle + \sigma_n^2)}. \tag{B5}$$

Here, a factor of $\langle|\widehat{U}(x,y)|^2\rangle$ in the numerator cancels the first term in the denominator. Thus, we arrive at the following relationship:

$$S_F = \frac{1}{1 + \frac{\sigma_n^2}{\langle|\widehat{U}_S(x,y)|^2\rangle}}, \tag{B6}$$

where it is apparent that the second term in the denominator is the inverse of the SNR S/N, since

$$S/N = \frac{\langle|\widehat{U}_S(x,y)|^2\rangle}{\sigma_n^2}. \tag{B7}$$

For all intents and purposes, we repeat Eq. (B7) above in Eq. (16).

REFERENCES

1. J. W. Goodman, D. W. Jackson, M. Lehmann, J. Knotts, and A. P. Profile, "Experiments in long-distance holographic imagery," Appl. Opt. **8**, 1581–1586 (1969).
2. J. W. Goodman, W. H. Huntley, D. W. Jackson, and M. Lehmann, "Wavefront-reconstruction imaging through random media," Appl. Phys. Lett. **8**, 311–313 (1966).

3. J. D. Gaskill, "Imaging through a randomly inhomogeneous medium by wavefront reconstruction," J. Opt. Soc. Am. A **58**, 600–608 (1968).
4. J. D. Gaskill, "Atmospheric degradation of holographic images," J. Opt. Soc. Am. **59**, 308–318 (1969).
5. J. W. Goodman, "Systems application of holography," Proc. SPIE **0015**, 1–8 (1968).
6. J. W. Goodman and R. W. Lawrence, "Digital image formation from electronically detected holograms," Appl. Phys. Lett. **11**, 77–79 (1967).
7. D. L. Fried, "Limiting resolution looking down through the atmosphere," J. Opt. Soc. Am. **56**, 1380–1384 (1966).
8. D. L. Fried, "Optical heterodyne detection of an atmospherically distorted signal wave front," Proc. IEEE **55**, 57–77 (1967).
9. J. P. Moreland and S. A. Collins, "Optical heterodyne detection of a randomly distorted signal beam," J. Opt. Soc. Am. **59**, 10–13 (1969).
10. R. K. Tyson, *Introduction to Adaptive Optics* (SPIE, 2011).
11. M. F. Spencer and D. E. Thornton, "Signal-to-noise models for digital- holographic detection," Proc. SPIE **1065**, 1065008 (2018).
12. J. D. Barchers, D. L. Fried, and D. J. Link, "Evaluation of the performance of Hartmann sensors in strong scintillation," Appl. Opt. **41**, 1012–1021 (2002).
13. J. D. Barchers, D. L. Fried, and D. J. Link, "Evaluation of the performance of a shearing interferometer in strong scintillation in the absence of additive measurement noise," Appl. Opt. **41**, 3674–3684 (2002).
14. D. L. Fried, "Branch point problem in adaptive optics," J. Opt. Soc. Am. A **15**, 2759–2768 (1998).
15. J. D. Barchers and T. A. Rhoadarmer, "Evaluation of phase-shifting approaches for a point-diffraction interferometer with the mutual coherence function," Appl. Opt. **41**, 7499–7509 (2002).
16. T. A. Rhoadarmer, "Development of a self-referencing interferometer wavefront sensor," Proc. SPIE **5553**, 1–15 (2004).
17. M. J. Steinbock, M. W. Hyde, and J. D. Schmidt, "LSPV+7, a branch-point-tolerant reconstructor for strong turbulence adaptive optics," Appl. Opt. **53**, 3821–3831 (2014).
18. T. J. Brennan and T. A. Rhoadarmer, "Performance of a woofer-tweeter deformable mirror control architecture for high-bandwidth high-spatial resolution adaptive optics," Proc. SPIE **6306**, 63060B (2006).
19. D. J. Wheeler and J. D. Schmidt, "Coupling of Gaussian Schell-model beams into single-mode optical fibers," J. Opt. Soc. Am. A **28**, 1224–1238 (2011).
20. M. F. Spencer, "Spatial heterodyne," in *Encyclopedia of Modern Optics*, 2nd ed. (Academic, 2018), Vol. **IV**, pp. 369–400.
21. D. E. Thornton, M. F. Spencer, and G. P. Perram, "Deep-turbulence wavefront sensing using digital holography in the on-axis phase shifting recording geometry," Proc. SPIE **10410**, 1041004 (2017).
22. T. C. Poon and J. P. Liu, *Introduction to Modern Digital Holography* (Cambridge University, 2014).
23. G. Nehmetallah, R. Aylo, and L. Williams, *Analog and Digital Holography with Matlab* (SPIE, 2015).
24. M. F. Spencer, R. A. Raynor, M. T. Banet, and D. K. Marker, "Deep-turbulence wavefront sensing using digital-holographic detection in the off-axis image plane recording geometry," Opt. Eng. **56**, 031213 (2016).
25. M. T. Banet, M. F. Spencer, and R. A. Raynor, "Digital-holographic detection in the off-axis pupil plane recording geometry for deep-turbulence wavefront sensing," Appl. Opt. **57**, 465–475 (2018).
26. B. E. A. Saleh and M. C. Teich, *Fundamentals of Photonics* (Wiley, 2007).
27. J. D. Schmidt, M. J. Steinbock, and E. C. Berg, "A flexible testbed for adaptive optics in strong turbulence," Proc. SPIE **8038**, 80380O (2011).
28. T. A. Rhoadarmer and L. M. Klein, "Design of a spatially phase shifted self-referencing interferometer wave front sensor," Proc. SPIE **6306**, 63060K (2006).
29. J. P. Liu, T. C. Poon, G. S. Jhou, and P. J. Chen, "Comparison of two-, three-, and four-exposure quadrature phase-shifting holography," Appl. Opt. **50**, 2443–2450 (2011).
30. E. L. Dereniak and G. D. Boreman, *Infrared Detectors and Systems* (Wiley, 1996).
31. T. A. Rhoadarmer and J. D. Barchers, "Noise analysis for complex field estimation using a self-referencing interferometer wave front sensor," Proc. SPIE **4825**, 215–227 (2002).
32. J. D. Schmidt, *Numerical Simulation of Optical Wave Propagation* (SPIE, 2010).
33. T. J. Brennen, P. H. Roberts, and D. C. Mann, *WaveProp: A Wave Optics Simulation System for use with MATLAB, User's Guide Version 1.3* (Optical Sciences, 2010).
34. T. J. Brennen and P. H. Phillips, *AOTools: The Adaptive Optics Toolbox for use with MATLAB, User's Guide Version 1.4* (Optical Sciences, 2010).
35. M. F. Spencer, I. V. Dragulin, D. S. Cargill, and M. J. Steinbock, "Digital holography wave-front sensing in the presence of strong atmospheric turbulence and thermal blooming," Proc. SPIE **9617**, 961705 (2015).
36. M. T. Banet, M. F. Spencer, R. A. Raynor, and D. K. Marker, "Digital holography wavefront sensing in the pupil-plane recording geometry for distributed-volume atmospheric aberrations," Proc. SPIE **9982**, 998208 (2016).
37. G. P. Perram, S. J. Cusumano, R. L. Hengehold, and S. Fiorino, *An Introduction to Laser Weapon Systems* (Directed Energy Professional Society, 2010).
38. M. T. Banet and M. F. Spencer, "Spatial-heterodyne sampling requirements in the off-axis pupil plane recording geometry for deep-turbulence wavefront sensing," Proc. SPIE **10410**, 104100E (2017).
39. M. S. Corley and T. A. Rhoadarmer, "Evaluation of phase-shifting techniques for a self-referencing interferometer wavefront sensor," Proc. SPIE **5894**, 58940R (2005).
40. T. R. Ellis, "Shack-Hartmann and interferometric hybrid wavefront sensor," Ph.D. dissertation (The Air Force Institute of Technology, 2011).
41. L. C. Andrews and R. L. Phillips, *Laser Beam Propagation Through Random Media*, 2nd ed. (SPIE, 2005).